PAPER

Dependence on plasma shape and plasma fueling for small edge-localized mode regimes in TCV and ASDEX Upgrade*

IOP Publishing | International Atomic Energy Agency Nuclear Fusion

Nucl. Fusion **59** (2019) 086020 (13pp) https://doi.org/10.1088/1741-4326/ab2211

Dependence on plasma shape and plasma fueling for small edge-localized mode regimes in TCV and ASDEX Upgrade*

B. Labit[15], T. Eich[35], G.F. Harrer[54], E. Wolfrum[35], M. Bernert[35], M.G. Dunne[35], L. Frassinetti[21], P. Hennequin[32], R. Maurizio[15], A. Merle[15], H. Meyer[5], S. Saarelma[5], U. Sheikh[15], J. Adamek[28], M. Agostini[8], D. Aguiam[29], R. Akers[5], R. Albanese[47], C. Albert[25], E. Alessi[22], R. Ambrosino[48], Y. Andrèbe[15], C. Angioni[35], G. Apruzzese[42], M. Aradi[25], H. Arnichand[15], F. Auriemma[8], G. Avdeeva[41], J.M. Ayllon-Guerola[43], F. Bagnato[15], V.K. Bandaru[35], M. Barnes[40,62], L. Barrera-Orte[18], P. Bettini[8], R. Bilato[35], O. Biletskyi[55], P. Bilkova[28], W. Bin[22], P. Blanchard[15], T. Blanken[16], V. Bobkov[35], A. Bock[35], D. Boeyaert[20], K. Bogar[28], O. Bogar[28], P. Bohm[28], T. Bolzonella[8], F. Bombarda[42], L. Boncagni[42], F. Bouquey[6], C. Bowman[52], S. Brezinsek[20], D. Brida[35], D. Brunetti[22], J. Bucalossi[6], J. Buchanan[5], J. Buermans[34], H. Bufferand[6], S. Buller[10], P. Buratti[42], A. Burckhart[35], G. Calabrò[59], L. Calacci[49], Y. Camenen[2], B. Cannas[11], P. Cano Megías[43], D. Carnevale[49], F. Carpanese[15], M. Carr[5], D. Carralero[33,35], L. Carraro[8], A. Casolari[28], A. Cathey[35], F. Causa[42], M. Cavedon[35], M. Cecconello[12], S. Ceccuzzi[42], J. Cerovsky[28], S. Chapman[7], P. Chmielewski[27], D. Choi[15], C. Cianfarani[42], G. Ciraolo[6], S. Coda[15], R. Coelho[29], L. Colas[6], D. Colette[6], L. Cordaro[8], F. Cordella[42], S. Costea[24], D. Coster[35], D.J. Cruz Zabala[43], G. Cseh[51], A. Czarnecka[27], I. Cziegler[52], O. D'Arcangelo[42], A. Dal Molin[22], P. David[35], G. De Carolis[49], H. De Oliveira[15], J. Decker[15], R. Dejarnac[28], R. Delogu[8], N. den Harder[36], M. Dimitrova[28], F. Dolizy[16], J.J. Domínguez-Palacios Durán[43], D. Douai[6], A. Drenik[35], M. Dreval[55], B. Dudson[52], D. Dunai[51], B.P. Duval[15], R. Dux[35], S. Elmore[5], O. Embréus[10], B. Erdõs[26], E. Fable[35], M. Faitsch[35], A. Fanni[11], M. Farnik[28], I. Faust[35], J. Faustin[36], N. Fedorczak[6], F. Felici[15], S. Feng[22], X. Feng[13], J. Ferreira[29], G. Ferrò[42], O. Février[15], O. Ficker[28], L. Figini[22], A. Figueiredo[29], A. Fil[52], M. Fontana[15], M. Francesco[49], C. Fuchs[35], S. Futatani[56], L. Gabellieri[42], D. Gadariya[33], D. Gahle[14], D. Galassi[15], K. Gałązka[27], J. Galdon-Quiroga[43], S. Galeani[52], D. Gallart[4], A. Gallo[2], C. Galperti[15], S. Garavaglia[22], J. Garcia[6], J. Garcia-Lopez[43], M. Garcia-Muñoz[43], L. Garzotti[5], J. Gath[41], B. Geiger[35], L. Giacomelli[22], L. Giannone[35], S. Gibson[15], L. Gil[29], E. Giovannozzi[42], G. Giruzzi[6], M. Gobbin[8], J. Gonzalez-Martin[43], T.P. Goodman[15], G. Gorini[45], M. Gospodarczyk[49], G. Granucci[22], D. Grekov[31], G. Grenfell[8], M. Griener[35], M. Groth[1], O. Grover[28], M. Gruca[27], A. Gude[35], L. Guimarais[29], T. Gyergyek[30], P. Hacek[28], A. Hakola[50], C. Ham[5], T. Happel[35], J. Harrison[5], A. Havranek[28], J. Hawke[15], S. Henderson[14], L. Hesslow[10], F. Hitzler[35], B. Hnat[40,62], J. Hobirk[35], M. Hoelzl[35], D. Hogeweij[19], C. Hopf[35], M. Hoppe[10], J. Horacek[28], M. Hron[28], Z. Huang[15,36], A. Iantchenko[15], D. Iglesias[5], V. Igochine[35], P. Innocente[8], C. Ionita-Schrittwieser[24], H. Isliker[3], I. Ivanova-Stanik[27], A. Jacobsen[5,35], M. Jakubowski[36], F. Janky[35], A. Jardin[5,27], F. Jaulmes[28],

* In the future we will refer to the author list of the paper as the EUROfusion MST1 Team

T. Jensen[41], T. Jonsson[21], A. Kallenbach[35], A. Kappatou[35], A. Karpushov[15], S. Kasilov[25], Y. Kazakov[34], P.V. Kazantzidis[38], D. Keeling[5], M. Kelemen[30], A. Kendl[24], W. Kernbichler[25], A. Kirk[5], G. Kocsis[51], M. Komm[28], M. Kong[15], V. Korovin[55], M. Koubiti[2], J. Kovacic[30], N. Krawczyk[27], K. Krieger[35], L. Kripner[28], A. Křivská[34], O. Kudlacek[35], Y. Kulyk[55], T. Kurki-Suonio[1], R. Kwiatkowski[57], F. Laggner[23], L. Laguardia[22], A. Lahtinen[46], P. Lang[35], J. Likonen[50], B. Lipschultz[52], F. Liu[58], R. Lombroni[59], R. Lorenzini[8], V.P. Loschiavo[47], T. Lunt[35], E. Macusova[28], J. Madsen[41], R. Maggiora[39], B. Maljaars[16], P. Manas[35], P. Mantica[22], M.J. Mantsinen[4,53], P. Manz[35], M. Maraschek[35], V. Marchenko[60], C. Marchetto[22], A. Mariani[22], C. Marini[15], T. Markovic[28], L. Marrelli[8], P. Martin[8], J.R. Martín Solís[33], A. Martitsch[25], S. Mastrostefano[17,48], F. Matos[36], G. Matthews[5], M.-L. Mayoral[18], D. Mazon[6], C. Mazzotta[42], P. Mc Carthy[44], K. McClements[5], R. McDermott[35], B. Mcmillan[7], C. Meineri[8], V. Menkovski[16], D. Meshcheriakov[35], M. Messmer[16], D. Micheletti[22], D. Milanesio[39], F. Militello[5], I.G. Miron[37], J. Mlynar[28], V. Moiseenko[55], P.A. Molina Cabrera[15], J. Morales[6], J.-M. Moret[15], A. Moro[22], D. Moulton[5], F. Nabais[29], V. Naulin[41], D. Naydenkova[28], R.D. Nem[41], F. Nespoli[2,6], S. Newton[5], A.H. Nielsen[41], S.K. Nielsen[41], V. Nikolaeva[29], M. Nocente[45], S. Nowak[22], M. Oberkofler[35], R. Ochoukov[35], P. Ollus[1], J. Olsen[41], J. Omotani[10], J. Ongena[25], F. Orain[35], F.P. Orsitto[17], R. Paccagnella[8], A. Palha[16], L. Panaccione[17], R. Panek[28], M. Panjan[30], G. Papp[35], I. Paradela Perez[1], F. Parra[40,62], M. Passeri[49], A. Pau[11,15], G. Pautasso[35], R. Pavlichenko[55], A. Perek[19], V. Pericoli Radolfini[48], F. Pesamosca[15], M. Peterka[28], V. Petrzilka[28], V. Piergotti[17], L. Pigatto[8], P. Piovesan[8], C. Piron[8], L. Piron[8,5], V. Plyusnin[29], G. Pokol[26], E. Poli[35], P. Pölöskei[26], T. Popov[61], Z. Popovic[33], G. Pór[26], L. Porte[15], G. Pucella[17], M.E. Puiatti[8], T. Pütterich[35], M. Rabinski[57], J. Juul Rasmussen[41], J. Rasmussen[41], G.A. Rattá[33], S. Ratynskaia[21], T. Ravensbergen[16], D. Réfy[51], M. Reich[35], H. Reimerdes[15], F. Reimold[20,36], D. Reiser[20], C. Reux[6], S. Reznik[30], D. Ricci[22], N. Rispoli[22], J.F. Rivero-Rodriguez[43], G. Rocchi[17], M. Rodriguez-Ramos[43], A. Romano[17], J. Rosato[32], G. Rubinacci[17], G. Rubino[8], D.A. Ryan[5], M. Salewski[41], A. Salmi[50], D. Samaddar[5], L. Sanchis-Sanchez[43], J. Santos[29], K. Särkimäki[1], M. Sassano[49], O. Sauter[15], R. Scannell[5], M. Scheffer[16], B.S. Schneider[24], P. Schneider[35], R. Schrittwieser[24], M. Schubert[35], J. Seidl[28], E. Seliunin[29], S. Sharapov[5], R.R. Sheeba[2], G. Sias[11], B. Sieglin[35], C. Silva[29], S. Sipilä[1], S. Smith[52], A. Snicker[1], E.R. Solano[33], S.K. Hansen[41], C. Soria-Hoyo[43], E. Sorokovoy[55], C. Sozzi[22], A. Sperduti[12], G. Spizzo[8], M. Spolaore[8], M. Stejner[41], L. Stipani[15], J. Stober[35], P. Strand[10], H. Sun[5,35], W. Suttrop[35], D. Sytnykov[55], T. Szepesi[51], B. Tál[51], T. Tala[50], G. Tardini[35], M. Tardocchi[22], A. Teplukhina[15], D. Terranova[8], D. Testa[15], C. Theiler[15], E. Thorén[21], A. Thornton[5], B. Tilia[42], P. Tolias[21], M. Tomes[28], M. Toscano-Jimenez[43], C. Tsironis[38], C. Tsui[15], O. Tudisco[42], J. Urban[28], M. Valisa[8], M. Vallar[8], P. Vallejos Olivares[21], M. Valovic[5], D. Van Vugt[16], B. Vanovac[19], J. Varje[1], J. Varju[28], S. Varoutis[31], S. Vartanian[6], O. Vasilovici[24], J. Vega[33], G. Verdoolaege[9], K. Verhaegh[15,52], L. Vermare[32], N. Vianello[8], J. Vicente[29], E. Viezzer[43], F. Villone[17], I. Voitsekhovitch[5], D. Voltolina[8], P. Vondracek[28], N.M.T. Vu[15], N. Walkden[5], T. Wauters[34], M. Weiland[35], V. Weinzettl[28], M. Wensing[15], S. Wiesen[20], M. Wiesenberger[24], G. Wilkie[10], M. Willensdorfer[35], M. Wischmeier[35], K. Wu[59], L. Xiang[41], R. Zagorski[27], D. Zaloga[57], P. Zanca[8], R. Zaplotnik[30], J. Zebrowski[57], W. Zhang[35], A. Zisis[38], S. Zoletnik[51] and M. Zuin[8]

[1] Department of Applied Physics, Aalto University, PO Box 14100, FI-00076 Aalto, Finland
[2] Aix-Marseille Université, CNRS, PIIM, F13013 Marseille, France
[3] Aristotle University of Thessaloniki, Thessaloniki, Greece
[4] Barcelona Supercomputing Center, Jordi Girona 29, 08034 Barcelona, Spain
[5] CCFE, Culham Science Centre, Abingdon, Oxon, OX14 3DB, United Kingdom of Great Britain and Northern Ireland
[6] CEA IRFM, F-13108 Saint Paul Lez Durance, France
[7] Department of Physics, Centre for Fusion, Space and Astrophysics, Warwick University, Coventry CV47AL, United Kingdom of Great Britain and Northern Ireland
[8] Consorzio RFX, Corso Stati Uniti 4, 35127 Padova, Italy
[9] Department of Applied Physics UG, Ghent University, St-Pietersnieuwstraat 41, B-9000 Ghent, Belgium
[10] Department of Earth and Space Sciences, Chalmers University of Technology, SE-41296 Gothenburg, Sweden
[11] Department of Electrical and Electronic Engineering, University of Cagliari, Piazza d'Armi 09123 Cagliari, Italy
[12] Department of Physics and Astronomy, Uppsala University, SE-75120 Uppsala, Sweden
[13] Department of Physics, Durham University, Durham, DH1 3LE, United Kingdom of Great Britain and Northern Ireland
[14] Department of Physics, University of Strathclyde, 107 Rottenrow, Glasgow G4 0NG, United Kingdom of Great Britain and Northern Ireland
[15] Ecole Polytechnique Fédérale de Lausanne (EPFL), Swiss Plasma Center (SPC), CH-1015 Lausanne, Switzerland
[16] Eindhoven, University of Technology, PO Box 513 NL-5600 MB Eindhoven, Netherlands
[17] ENEA/CREATE, DIEI, Università di Cassino, Via Di Biasio 43, 03043, Cassino (FR), Italy
[18] EUROfusion PMU, Boltzmannstraße 2, 85748, Garching, Germany
[19] FOM Institute DIFFER, Dutch Institute for Fundamental Energy Research, Netherlands
[20] Forschungszentrum Jülich GmbH, Institut für Energie- und Klimaforschung-Plasmaphysik, 52425 Jülich, Germany
[21] Fusion Plasma Physics, EES, KTH, SE-10044 Stockholm, Sweden
[22] IFP-CNR, Via R. Cozzi 53, 20125 Milano, Italy
[23] Institut für Angewandte Physik, Technische Universität Wien, Wiedner Hauptstraße 8-10, 1040 Wien, Austria
[24] Institut für Ionen- und Angewandte Physik, Universität Innsbruck, Technikerstraße 25, 6020 Innsbruck, Austria
[25] Institut für Theoretische Physik, Technische Universität Graz, 8010 Graz, Austria
[26] Institute of Nuclear Techniques, Budapest University of Technology and Economics, PO Box 91, H-1521 Budapest, Hungary
[27] Institute of Plasma Physics and Laser Microfusion, Hery 23, 01-497 Warsaw, Poland
[28] Institute of Plasma Physics AS CR, Za Slovankou 1782/3, 182 00 Praha 8, Czech Republic
[29] Instituto de Plasmas e Fusão Nuclear, Instituto Superior Técnico, Universidade de Lisboa, Lisbon, Portugal
[30] Jožef Stefan Institute, Jamova 39, SI-1000 Ljubljana, Slovenia
[31] Karlsruhe Institute of Technology, PO Box 3640, D-76021 Karlsruhe, Germany
[32] Laboratoire de Physique des Plasmas, CNRS UMR7648, Ecole Polytechnique, 91128 Palaiseau, France
[33] Laboratorio Nacional de Fusión, CIEMAT, Madrid, Spain
[34] Laboratory for Plasma Physics Koninklijke Militaire School, Ecole Royale Militaire Renaissancelaan 30 Avenue de la Renaissance B-1000, Brussels, Belgium
[35] Max-Planck-Institut für Plasmaphysik, D-85748 Garching, Germany
[36] Max-Planck-Institut für Plasmaphysik, Teilinstitut Greifswald, D-17491 Greifswald, Germany
[37] National Institute for Laser, Plasma and Radiation Physics, PO Box MG-36, Bucharest, Romania
[38] National Technical University of Athens, Athens, Greece
[39] Dipartimento di Elettronica e Telecomunicazioni (DET), Politecnico di Torino, Torino, Italy
[40] Rudolf Peierls Centre for Theoretical Physics, University of Oxford, Oxford, United Kingdom of Great Britain and Northern Ireland
[41] Department of Physics, Technical University of Denmark, Bldg 309, DK-2800 Kgs Lyngby, Denmark
[42] Unità Tecnica Fusione, ENEA C. R. Frascati, via E. Fermi 45, 00044 Frascati (Roma), Italy
[43] Universidad de Sevilla. C/ S. Fernando, 4, C.P. 41004-Sevilla, Spain
[44] University College Cork (UCC), Cork, Ireland
[45] University Milano-Bicocca, Piazza della Scienza 3, 20126 Milano, Italy
[46] Department of Physics, University of Helsinki, PO Box 64, FI-00014 University of Helsinki, Finland
[47] University of Napoli 'Federico II', Consorzio CREATE, Via Claudio 21, 80125 Napoli, Italy
[48] University of Napoli Parthenope, Consorzio CREATE, Via Claudio 21, 80125 Napoli, Italy
[49] University of Rome Tor Vergata, Via del Politecnico 1, 00133 Rome, Italy

[50] VTT Technical Research Centre of Finland, PO Box 1000, FI-02044 VTT, Finland
[51] Wigner Research Centre for Physics, PO Box 49, H-1525 Budapest, Hungary
[52] Department of Physics, York Plasma Institute, University of York, Heslington, York, YO10 5DD, United Kingdom of Great Britain and Northern Ireland
[53] ICREA, Pg. Lluís Companys 23, 08010 Barcelona, Spain
[54] Institute of Applied Physics, TU Wien, Fusion@OEAW, Vienna, Austria
[55] Kharkov Institute of Physics and Technology, National Science Center, 61108, Kharkiv, Ukraine
[56] Universitat Politècnica de Catalunya, ES—08028, Barcelona, Spain
[57] NCBJ National Centre for Nuclear Research, PL—05-400, Otwock, Poland
[58] Université de Nice Sophia Antipolis, FR—06103, Nice, France
[59] Universitá Tuscia, IT—01100, Viterbo, Italy
[60] Fusion Theory Division, Institute for Nuclear Research of NAS, UA—3028, Kyiv, Ukraine
[61] Faculty of Physics, St. Kliment Ohridski University, BG—1784, Sofia, Bulgaria
[62] Culham Centre for Fusion Energy, Abingdon, United Kingdom of Great Britain and Northern Ireland

E-mail: benoit.labit@epfl.ch

Received 31 January 2019, revised 3 May 2019
Accepted for publication 16 May 2019
Published 26 June 2019

Abstract

Within the EUROfusion MST1 work package, a series of experiments has been conducted on AUG and TCV devices to disentangle the role of plasma fueling and plasma shape for the onset of small ELM regimes. On both devices, small ELM regimes with high confinement are achieved if and only if two conditions are fulfilled at the same time. Firstly, the plasma density at the separatrix must be large enough ($n_{e,sep}/n_G \sim 0.3$), leading to a pressure profile flattening at the separatrix, which stabilizes type-I ELMs. Secondly, the magnetic configuration has to be close to a double null (DN), leading to a reduction of the magnetic shear in the extreme vicinity of the separatrix. As a consequence, its stabilizing effect on ballooning modes is weakened.

Keywords: H-mode, type-II ELMs, grassy ELMs, plasma triangularity, separatrix density, ballooning modes

(Some figures may appear in colour only in the online journal)

1. Introduction

To achieve its goals, ITER has to operate in the H-mode confinement regime, specified within the ITER baseline scenario (IBS) [1] for which the key parameters are shown in figure 1. Such scenario with good confinement is expected to be accompanied with large type-I ELMs. Therefore, if unmitigated, the resulting peak heat fluxes will exceed the material limits of $\simeq$10 MW $\cdot$ m^{-2} in ITER size devices and even more so in a demonstration fusion power plant (DEMO). An attractive solution to overcome this limitation is to operate in the H-mode confinement regime with small ELMs such as type-II or grassy ELMs [2–6], for which the good confinement is maintained w.r.t. to the type-I regime.

Historically, a distinction has been made between type-II and grassy ELMs: On the one hand, type-II ELMs are observed when increasing the plasma density, edge safety factor and triangularity, moving the plasma close to a double-null (DN) configuration. In addition, the onset of type-II ELMs is accompanied by a broadband fluctuation in the range of 30–50 kHz, observed in the magnetics, microwave reflectometry and electron cyclotron emission diagnostic up to the pedestal top ($0.7 < \rho_{pol} < 0.95$). On the other hand, the grassy ELM regime was found on JT-60U with increased triangularity

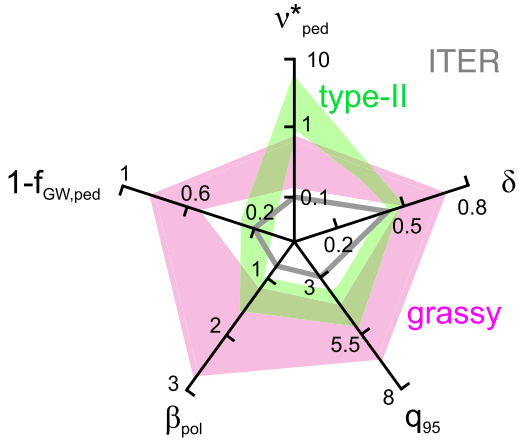

Figure 1. Main pedestal top parameters defining the ITER baseline scenario (grey line). The range of these parameters for grassy (pink) and type-II (green) ELMs are also given. Reproduced from [6].

and high edge safety factor, but at low collisionality, close to ITER-relevant values. And no signature of broadband turbulence has been reported for this ELM regime. The distinction between type-II and grassy ELMs is highlighted in figure 1 where the typical values of the IBS key parameters are shown.

Nevertheless, it is not clear if the IBS parameters are the key parameters to fulfill to achieve a small ELM regime or if there exist other key ingredients in addition to q_{95} and δ in common between type-II and grassy ELM regimes. It is also of great importance to further assess if a small ELM regime would be achieved in ITER under certain circumstances.

This paper summarizes the results of a series of experiments, conducted in AUG and in TCV to disentangle the role of plasma fueling, plasma triangularity and closeness to the DN configuration for the onset of a small ELM regime, either type-II or grassy (hereafter, the distinction is dropped on purpose). The necessity of a large density at the separatrix is demonstrated in section 2, while in section 3, the crucial role of the plasma shape is reported. A physical interpretation, suggesting a prominent role of the magnetic shear is given in section 4 followed by concluding remarks and outlook (section 5).

2. Small ELM regimes and plasma density at the separatrix

2.1. Pellet fueling versus gas fueling in AUG plasmas

In AUG #34462, a small ELM regime is reached at $t = 3.0$ s with strong gas fueling and a plasma shape close to a DN configuration (figure 2). The closeness to a DN configuration is monitored by the parameter $\Delta_{\rm sep}$, the distance, at the outboard midplane, between the separatrix and the flux surface through the secondary X-pt ($\Delta_{\rm sep}^{\#34462} = 7$ mm). At $t = 4.0$ s, while the plasma shape is unchanged, the gas fueling is replaced by pellet injection into the plasma core, maintaining the averaged plasma density. It is observed that the small ELMs are suppressed and the type-I ELMs are fully restored, as clearly seen on the divertor shunt current measurement.

Figure 3 shows the electron density and electron temperature profiles, from the Thomson scattering diagnostics, for both ELMy phases: small in red and type-I in black. Profiles have been shifted such that $T_{\rm e,sep} = 100$ eV (see section 4). The core fuelling with pellets has almost no effect on the temperature profiles (both $T_{\rm e}$ and $T_{\rm i}$). For the plasma density, the core profile is unchanged up to the pedestal top with $f_{G,\rm ped} \simeq 0.85$. The pressure gradient in the pedestal is almost unchanged. Conversely, the scrape-off layer (SOL) profile is strongly affected by the change in the fueling method: while the profile is broad with $f_{G,\rm sep} \simeq 0.3$ for strong gas fueling case (small), it becomes narrower for the pellet fueling case and the separatrix density is reduced by a factor of 2 ($4 \times 10^{19} \rightarrow 2 \times 10^{19}$ m^{-3}). This is further confirmed with the estimate of the fall-off lengths in the near SOL: with gas fueling, $\lambda_{n_{\rm e}}$ is increased by more than a factor of 2 and $\lambda_{p_{\rm e}}$ increases by 33%. A reduced pressure gradient around the separatrix means that the pedestal width is shrunk which in turn increases the stability of type-I ELMs. Further details on this scenario can be found in [7].

It has been observed on MAST [8] that the filamentary transport at the foot of the pedestal is significantly changed from type-I to type-II. Also, for AUG #34462, a change in the turbulent transport is revealed from Doppler back scattering measurements just inside the separatrix ($\rho_{\rm pol} \sim 0.99$). Figure 4 shows a 500 μs long time series of DBS signals (real part) measured within both phases. For the small ELM regime (DN and gas fueling, red), the DBS signal shows large bursts in amplitude. These bursts, in the range of 40–80 kHz, are much more frequent than in between type-I ELMs later in the discharge (close to DN and pellet fueling, black) [9]. Further investigations are needed to clarify the change in the turbulent transport between both ELM regimes but it suggests a correlation with the filamentary transport in the scrape-off layer close to the H-mode density limit [10].

2.2. Gas fueling scan in ELMy H-mode in TCV

A reliable scenario for type-I ELMy H-mode in TCV is obtained with the following parameters: lower single null, $I_{\rm p} = 140$ kA, $B_T = 1.4$ T, $\kappa = 1.5$, $\delta = 0.38$, $\Delta_{\rm sep} = 24$ mm, $q_{95} = 4.5$, $P_{\rm NBI} = 1$ MW ($P_{L-H} \sim 0.7$ MW at $n_{\rm e,av} = 3 \times 10^{19}$ m^{-3}). This scenario is illustrated in figure 5 for TCV #57103 (black traces). Even though the gas fueling is negligible, the plasma density is maintained constant by sufficient wall recycling from the carbon wall. The ELMs are monitored with a photodiode measuring the D_α radiation along a vertical line-of-sight. The pedestal profiles are

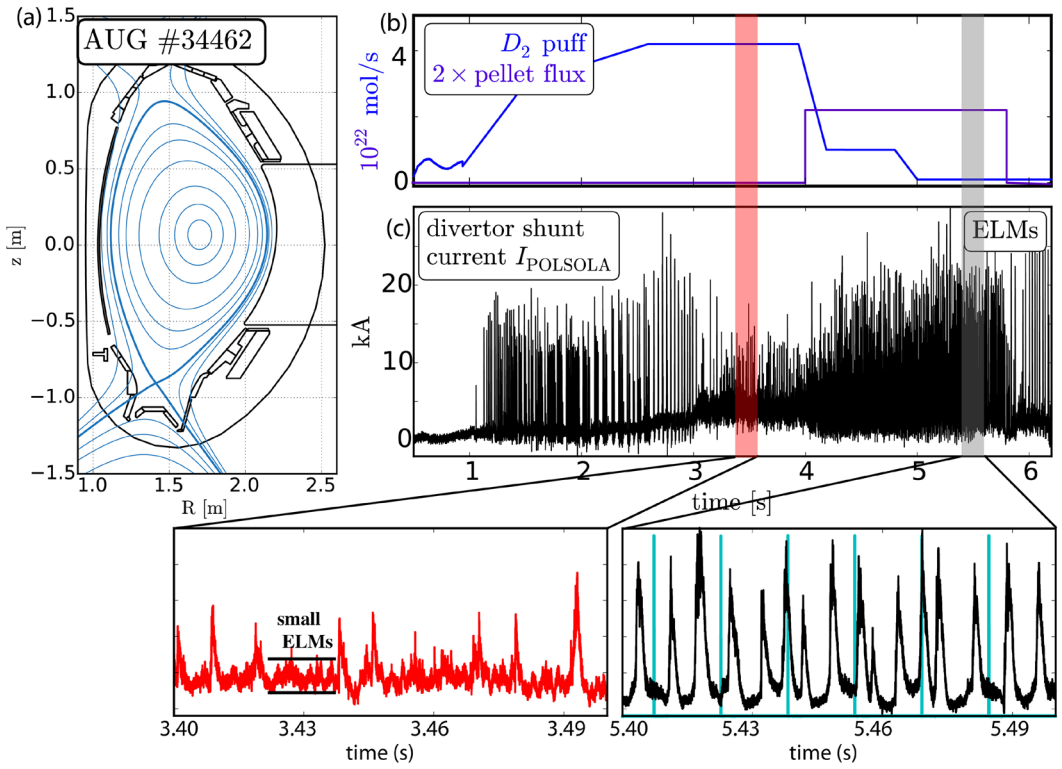

Figure 2. Summary of AUG #34462. Details can be found in [7].

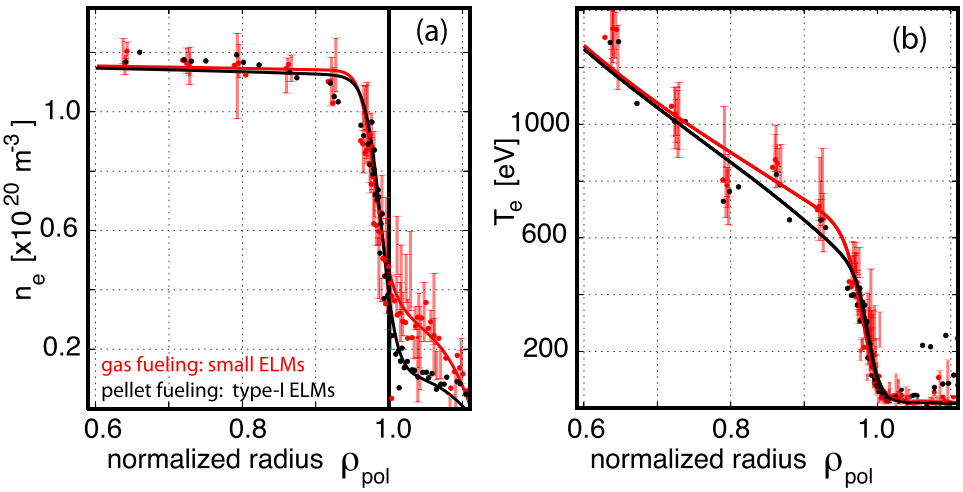

Figure 3. Kinetic profiles for AUG #34462 during the small ELMs phase with strong gas fueling (red) and during the type-I ELMy phase with pellet fueling (black).

obtained from a recently upgraded Thomson scattering system [11] then fitted with a modified hyperbolic tangent function [12] and shifted such that $T_{e,sep} = 50$ eV (see section 4). This scenario has been used to investigate the effect of gas fueling and impurity seeding on the pedestal structure and the energy confinement [13, 14].

As seen from the ASDEX-Upgrade experiment reported above, a key ingredient to achieve a small ELM regime is to operate at sufficiently large density at the separatrix ($f_{G,sep} \sim$ 0.3) which can be controlled via gas fueling. A mix of type-I and small ELM has been realized in TCV. Indeed, starting from the reference type-I ELM regime, a scan in deuterium fueling has been performed on a shot to shot basis [13, 14]. A summary of TCV #57105 for the largest fueling rate is given in figure 5 (red traces). As the D_2 flow increases, the following observations can be made (table 1):

(i) The type-I ELM frequency decreases by a factor of 2 while the relative loss energy $\Delta W/W$ remains around 11%;

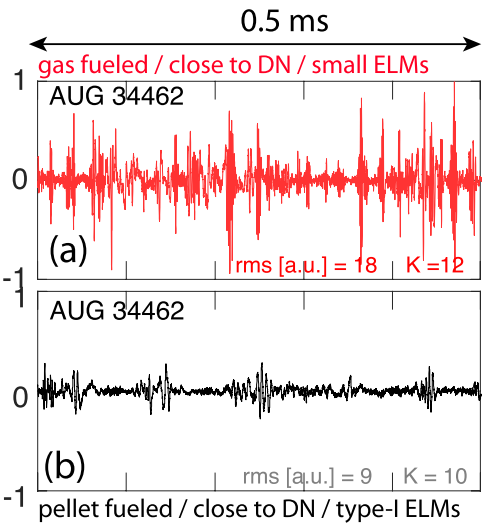

Figure 4. AUG #34462: Real part of the Doppler backscattering signal, measured at $\rho_{\mathrm{pol}} = 0.99$; (*a*) during 0.5 ms in the small ELMs phase (*b*) during 0.5 ms in between type-I ELMs.

(ii) The baseline level of the D_α signal increases which might indicate an elevation of the recycling level.
(iii) Small ELMs, in between type-I, are becoming more and more frequent. Their typical frequency is about 2.5 kHz.

A consequence of the reduced type-I ELM frequency is that the plasma density is not controlled anymore and it increases with time, eventually leading to a back transition into L-mode. The lost energy associated with each small ELM is below 1% which corresponds to the diagnostic resolution. In addition, no clear trend is found between the pedestal pressure height variations and the changes in the plasma stored energy when the fueling rate is varied [13]. The density growth at the pedestal is less rapid than the separatrix density elevation. As a consequence the ratio $n_{\mathrm{e,sep}}/n_{\mathrm{e,ped}}$ increases by a factor 2 from 0.25 to 0.5 (figure 6(*a*)). Despite the fact that the wall recycling is increased, no significant carbon accumulation in the plasma core is observed leading to a reduced fraction of core radiation with gas fueling.

An outward shift of the density pedestal, together with a reduction of the pedestal widths, are observed with increased fueling (figure 6(*b*)). Both effects are leading to a reduction of the peeling-ballooning stability for type-I ELMs. In addition, for this scenario with low shaping, no evidence of a high density front at the high field side [15] is reported so far from TCV, conversely to AUG. This might be due to the TCV open divertor geometry and will be reassessed once the TCV divertor is closed with baffles [16].

Finally, since no broadband turbulence has been observed on the magnetic probes, it cannot be concluded that these small ELMs are type-II. Nevertheless, a similar fueling scan for plasmas at higher triangularity, discussed in [13], also shows a transition to a mixed ELM regime, with, in this case, a signature of turbulence in the frequency range [20–40] kHz on the magnetics.

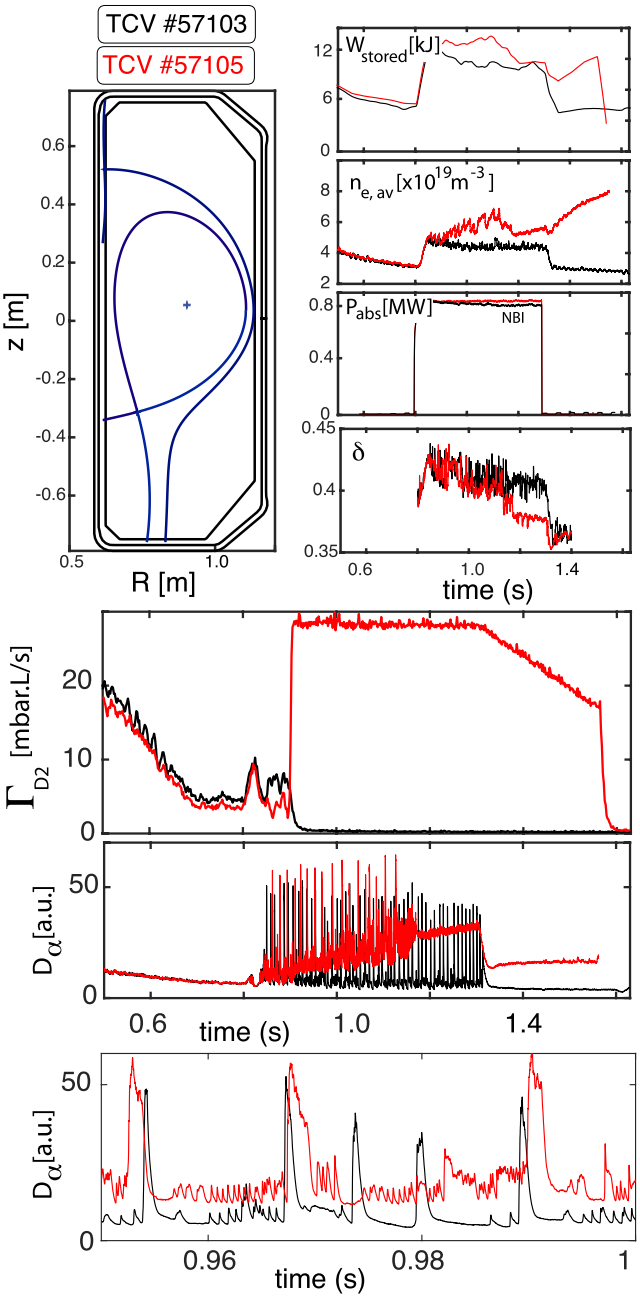

Figure 5. Overview of TCV shots 57103 ($\Gamma_{D2} = 0, H_{98y2} = 1.13$) and 57105 ($\Gamma_{D2} = 28$ mbar $\cdot$ L s^{-1}, $H_{98y2} = 1.06$) showing how type-I ELMs frequency is reduced with strong fueling.

3. Small ELM regime accessibility with plasma shaping

3.1. Small ELM regime for plasma with high triangularity in TCV

Type-II and/or grassy ELMs are usually observed at large plasma triangularity [4, 5, 17, 18]. A small ELM regime with controlled plasma density has been achieved in TCV. Two discharges (LSN, $I_{\mathrm{p}} = 170$ kA, $B_T = 1.4$ T) have been performed with the exact same parameters except the upper

Table 1. Summary of fueling scan of type-I ELMy H-mode in TCV with $q_{95} = 4.5$, $\delta = 0.4$, $P_{NB} = 1$ MW.

Γ_{D2} (mbar L s^{-1})	f_{ELM} (Hz)	$\frac{\Delta W}{W}$ (%)	$T_{e,ped}$ (eV)	W_{MHD} (kJ)	P_{rad} (kW)	$f_{rad,core}$ (%)
0	103 ± 21	11 ± 1	203 ± 12	10 ± 0.3	187 ± 7	34 ± 3
5	109 ± 29	10 ± 2	144 ± 9	11 ± 0.4	190 ± 13	32 ± 6
15	96 ± 38	11 ± 3	185 ± 5	12 ± 0.4	230 ± 13	30 ± 4
28	65 ± 14	12 ± 1	147 ± 7	13 ± 0.5	239 ± 12	31 ± 3

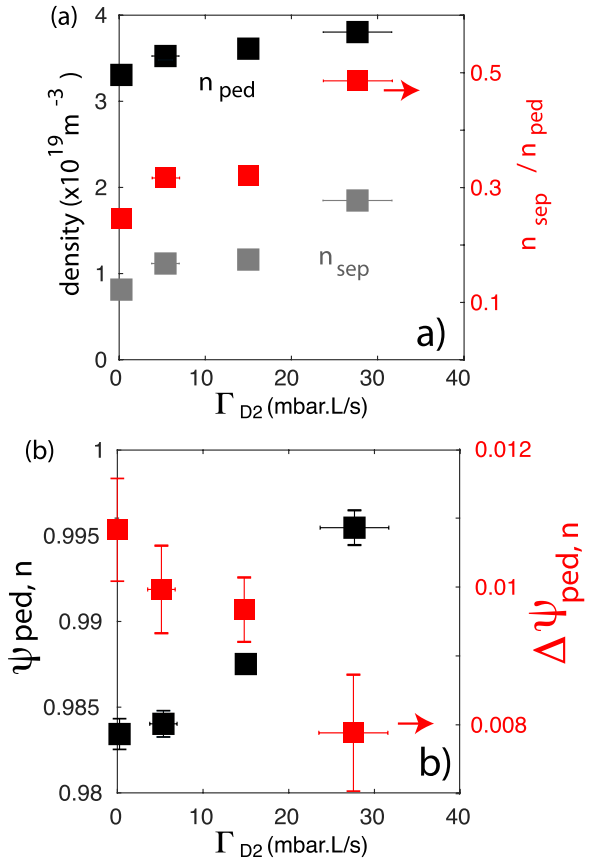

Figure 6. Main results of the D_2 fueling scan (*a*) Pedestal density (black); separatrix density (gray) and their ratio (red); (*b*) Pedestal locations (black) and widths (red).

triangularity which changes from $\delta_u = 0.1$ (#61057, $\delta = 0.4$, $\Delta_{sep} = 24$ mm) to $\delta_u = 0.32$ (#61056, $\delta = 0.54$, $\Delta_{sep} = 3$ mm) as shown in figure 7.

Both plasmas are heated with 1MW of NBI plus 0.75 MW of X3 ECRH. The same constant D_2 flow (3.8 mbar · L s^{-1}) has been imposed at the L-H transition giving $f_{G,ped} \simeq 0.35$. For the medium triangularity discharge, the ELMs are large type-I ELMs ($f_{ELM} = 100$ Hz, $\Delta W/W \sim 10\%$) while for the high triangularity discharge, type-I ELMs are fully suppressed and replaced by small high frequency ELMs for which $\Delta W/W < 1\%$.

Later in the discharge, the fuelling was increased by a factor of 8, resulting for the high triangularity case, to an increase of the plasma density up to an H-mode density limit disruption. For the medium triangularity shape, the type-I ELM frequency decreases so the density increases and a back-transition to L-mode is observed.

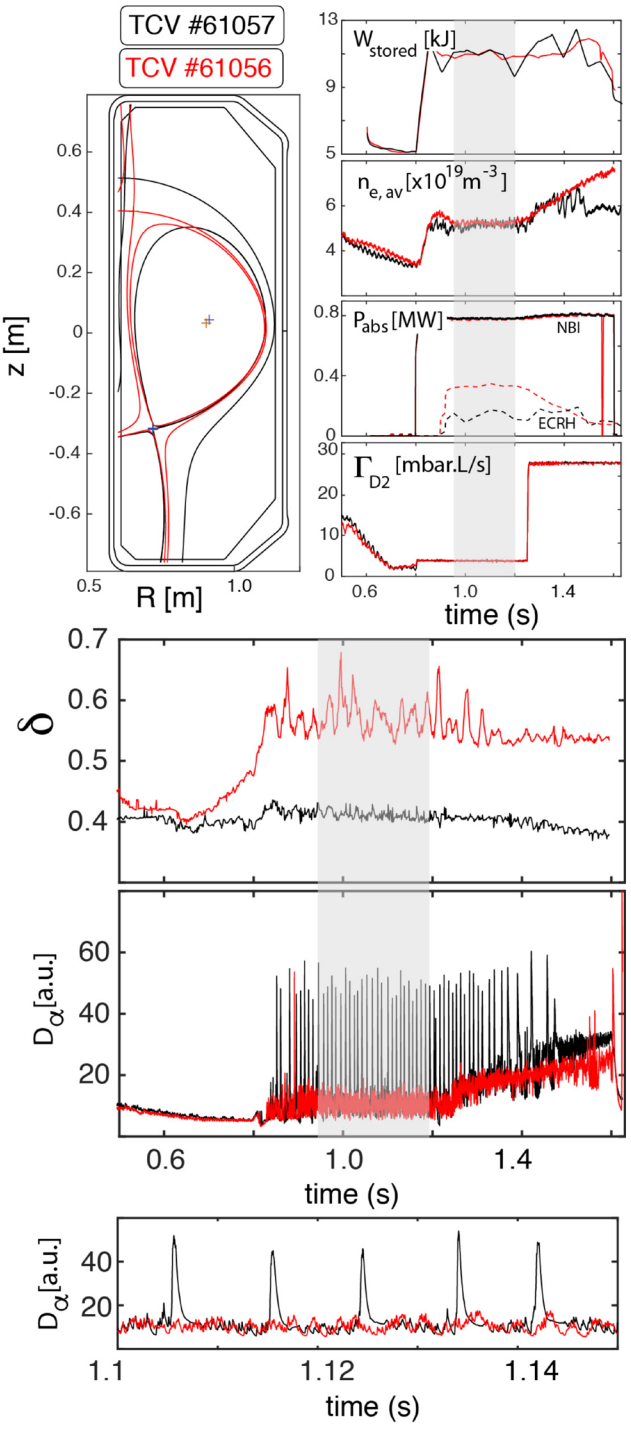

Figure 7. Overview of TCV #61057 ($\delta = 0.4 \Leftrightarrow \Delta_{sep} = 24$ mm, black) and #61056 ($\delta = 0.54 \Leftrightarrow \Delta_{sep} = 3$ mm , red) showing how type-I ELMS are fully stabilized close to a DN configuration.

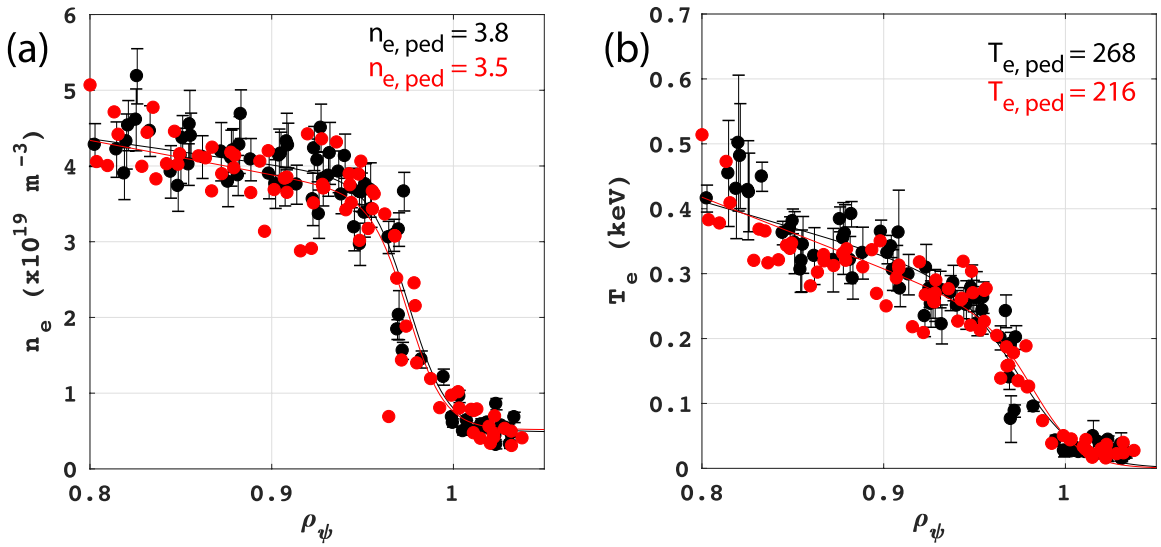

Figure 8. Kinetic profiles from the Thomson scattering diagnostic for TCV #61057 ($\delta = 0.4$, black) and #61056 ($\delta = 0.54$, red) together with the associated *mtanh* fits.

Table 2. Plasma and pedestal parameters comparing the type-I and small ELM regimes at TCV. They have been averaged over the time window indicated by the shaded area in figure 7.

ELM regime	q_{95}	δ	Δ_{sep} (mm)	$n_{e,sep}$ ($\times 10^{19}$ m^{-3})	$\nu_{\star,ped}$	β_{pol}	$f_{G,ped}$	W_{MHD} (kJ)	H_{98y2}
Type-I	4.7	0.38	24	0.9	2.66	1.13	0.34	11	1.0
Small	4.7	0.54	3	0.8	1.95	1.13	0.32	11	0.95

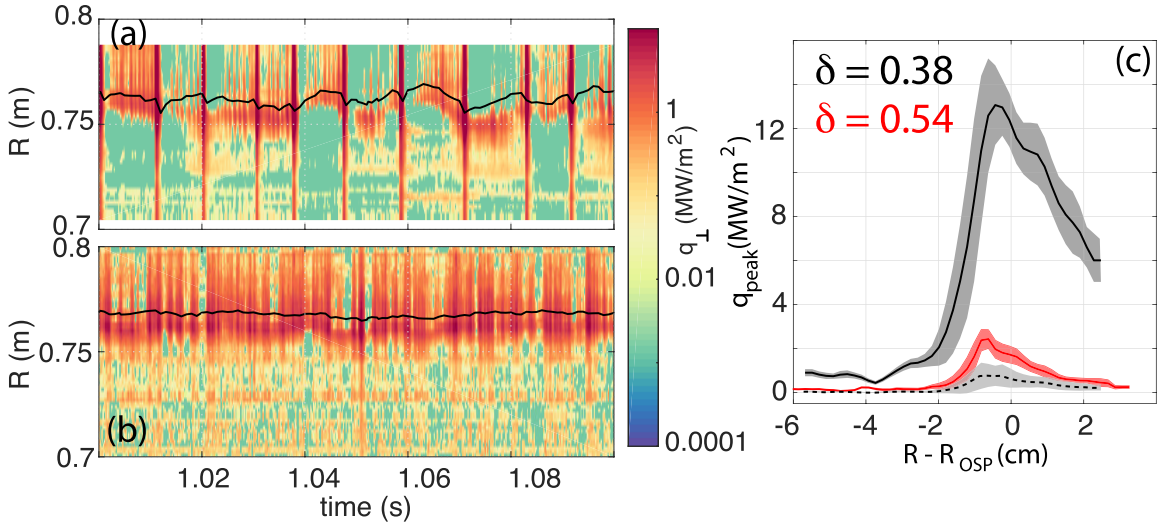

Figure 9. Outer target heat loads measured with IR thermography for (*a*) TCV #61057 (type-I ELMs); (*b*) TCV #61056 (small ELMs); The black line in (*a*) and (*b*) is the outer strike point locations according to the magnetic reconstruction; (*c*) Peak heat flux for type-I (black), small (red) and in between type-I ELMs (black; dashed).

Although, at low fueling rate, the plasma confinement usually improves when the triangularity is increased [18], here, the stored energy is the same for both triangularities and the density is perfectly well controlled in both situations. In figure 8, the temperature and density pedestal profiles are plotted. They are remarkably similar for both discharges even though the kinetic profiles are selected in the [75%–90%] phase of the type-I ELM cycle while they are time averaged for the small ELM case. As a consequence, the pedestal pressure is only increased by less than 5% for the large δ case. Some plasma and pedestal parameters are compared in table 2.

An expected benefit of the small ELM regime is a reduction of the peak heat loads at the targets. For both plasmas, a preliminary analysis of the heat loads at the outer strike point has been performed from infrared measurements [19]. Figure 9 shows the perpendicular heat flux along the outer target as a function of time. Compared to the type-I regime, the peak heat flux is reduced by a factor of about 10 with the

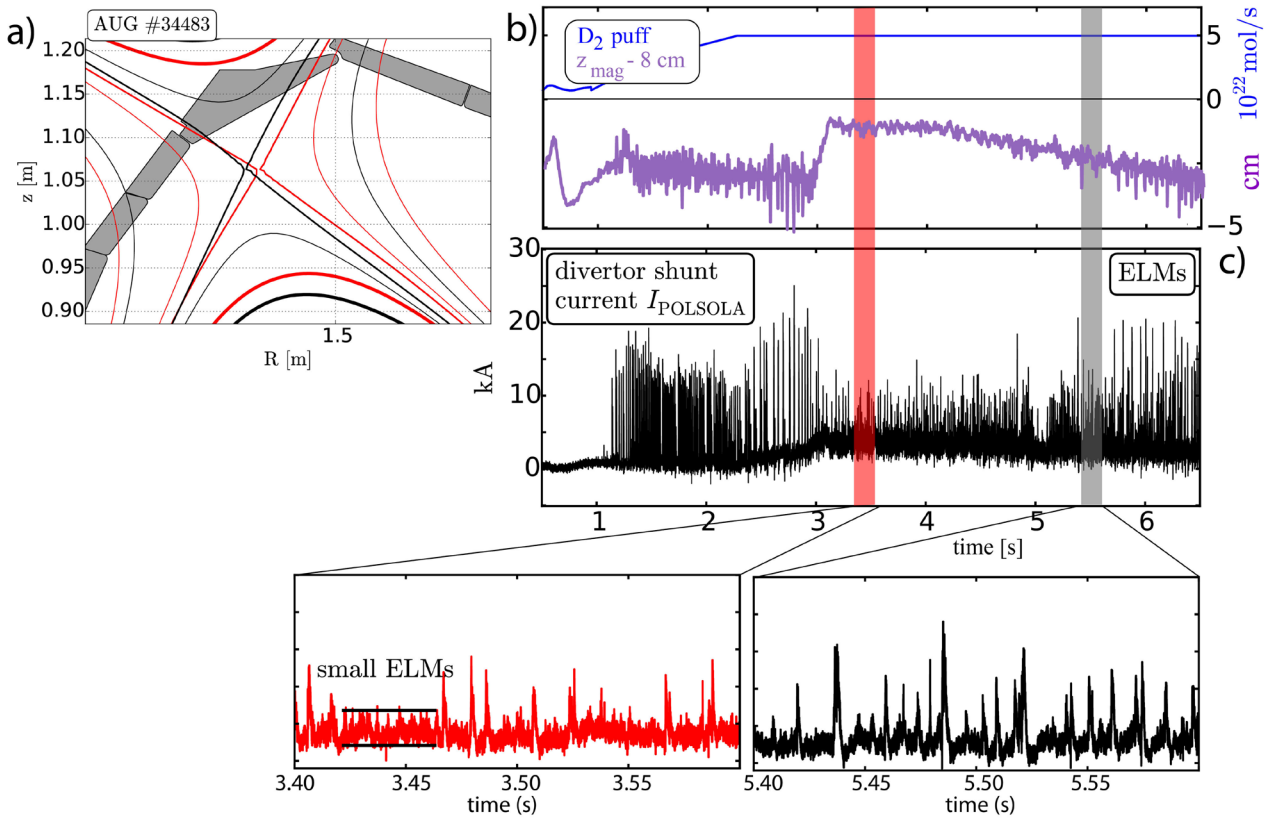

Figure 10. Summary of AUG #34483; (*a*) Close look at the magnetic equilibrium around the 2nd X-point xat $t = 3.5$ s (red) and $t = 5.5$ s (black); (*b*) D_2 fueling (blue) and vertical position of the magnetic axis (purple); (*c*) divertor shunt current showing that type-I ELMs are progressively restaured when the closeness to DN is relaxed.

small ELM regime, reaching similar levels as the inter-type-I ELM periods. In addition, compared to the value evaluated in between type-I ELMs, the time averaged heat flux decay length λ_q for the small ELM case is about 20% larger (6.5 mm versus 5.5 mm) and can be seen as a possible indication of an enhanced cross-field transport in the SOL. However, the uncertainty on the heat transmission for co-deposited surface layers ($\alpha_{sl} = 160$ kW m^{-2} K^{-1} here), in particular for graphite tiles [20] requires further detailed analysis and will be addressed in future work.

3.2. Effect of closeness to double-null on the small ELM regime in AUG

In AUG, the role of the SOL density has been revisited [7]. Indeed, it turns out that a large separatrix density ($f_{G,\mathrm{sep}} \sim 0.3$) is not a sufficient condition to achieve the small ELM regime. This has been demonstrated in AUG #34483 (figure 10). A small ELM regime is obtained with a constant large gas fueling, in a shape close to DN ($\Delta_{\mathrm{sep}} = 7$–$9$ mm). After $t = 4.0$ s, the plasma is progressively shifted down, relaxing the closeness to DN ($\Delta_{\mathrm{sep}} = 14$ mm) at almost constant triangularity δ and elongation κ. As the plasma is moved down, type-I ELMs are progressively restored, leading to a mix of ELM types. As for the TCV case discussed earlier, it is observed that the pedestal profiles are almost unchanged for both phases. Not only the pedestal top profiles are unchanged, but also the SOL profiles remain unaffected by the transition from small ELM to a mix of small and type-I ELMs.

4. Physical interpretation

The experimental results from AUG and TCV are consistent within each other and can be summarized as follows: a small ELM regime at high confinement can be achieved *if and only if* two conditions are fulfilled at the same time: the separatrix density is large enough: $f_{G,\mathrm{sep}} \geqslant 0.35$ and the plasma shape is close to a double-null configuration. In the following, the physical implications are discussed, starting with the pedestal stability analysis.

For the AUG and TCV plasmas discussed in section 3, the pedestal stability is analyzed using CLISTE and MISHKA codes for AUG [15] and CHEASE and KINX for TCV plasmas [21], respectively. The experimental T_{e} and n_{e} profiles are fitted with a modified hyperbolic tangent function [12]. Since the equilibrium reconstruction has uncertainties and the absolute pedestal position cannot be determined within an accuracy of ~5 mm, the profile location relative to the separatrix is assigned based on power flow [22]. From the two-point model [23], a typical value for the separatrix temperature is $T_{\mathrm{e,sep}} = 100$ eV for AUG [24], while one finds $T_{\mathrm{e,sep}} = 50$ eV for TCV. In addition, because of the steep gradients in the pedestal, an uncertainty of 10%–20% in $T_{\mathrm{e,sep}}$ does not impact on the pedestal location significantly. So, the temperature profiles

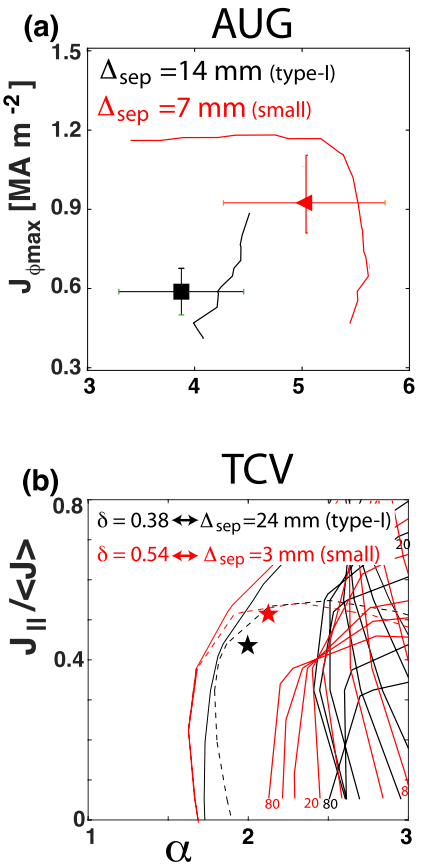

Figure 11. Stabiliy analysis of the pedestal; (*a*) Experimental points for AUG and peeling-ballooning boundary computed with CLISTE and MISHKA; (*b*) Experimental points for TCV and peeling-ballooning boudaray (thick solid), infinite *n* ballooning boundary at most unstable location (thin solid) and infinite *n* ballooning boundary at max. p' location computed (thin dashed) with CHEASE and KINX.

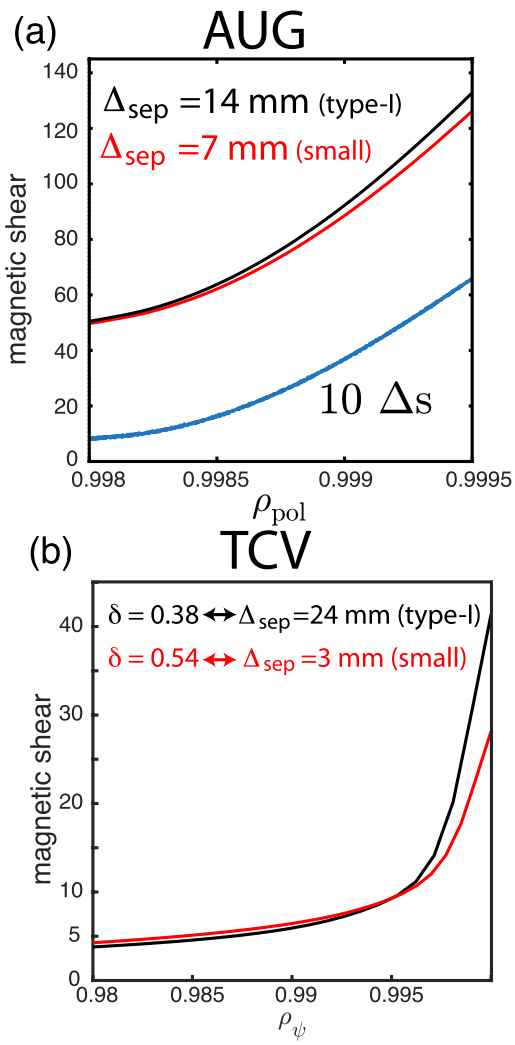

Figure 12. Magnetic shear profiles (*a*) for AUG plasmas (taken from [7]) and (*b*) for TCV plasmas.

are shifted in order to match these values at the separatrix and the density profiles are shifted by the same amount. The $j-\alpha$ stability diagrams are shown in figure 11. Here, j is the current density and α is the normalized pedestal pressure gradient. As expected, for the type-I ELMy cases (low shaping), the experimental pedestal pressure and current are close to the peeling-ballooning stability boundary. When plasmas are strongly shaped towards DN and small ELMs achieved, the intermediate-*n* peeling-ballooning boundary expands considerably. Nevertheless, the experimental pedestals are still close to this boundary, meaning that the pressure gradient and possibly, the edge current density are increased in both devices when a small ELM regime is achieved.

In addition to the dependence on the separatrix density, the onset of a small ELM regime depends on the closeness to the DN configuration. For both devices, a magnetic equilibrium, taking into account the pedestal bootstrap current self-consistently has been computed for type-I and small ELM regimes. The CLISTE code for AUG and the CHEASE code [25] for TCV cases are used, respectively. Figure 12 shows the resulting magnetic shear profile which has been flux surface averaged. It turns out that when the closeness to DN is relaxed, the magnetic shear in the immediate vicinity of the separatrix is larger than for the configuration close to DN. It is also known that ballooning modes with high toroidal mode numbers and driven by the local pressure gradient can be destabilized by a reduced magnetic shear [26, 27]. Therefore, we are conjecturing that small ELMs might be ballooning modes driven unstable in the vicinity of the separatrix. Such modes have high toroidal mode numbers and are therefore radially narrow, driven by the local pressure gradient and stabilized by magnetic shear.

The experimental results from AUG and TCV presented in this paper are in line with our current understanding about the physical mechanism which drives small (either type-II or grassy) ELMs. It can be summarized as follows:

- With strong plasma shaping (short Δ_{sep} and/or high δ), ballooning modes, driven by the pressure gradient are destabilized in the immediate vicinity of the separatrix where the magnetic shear is locally reduced.
- With strong plasma fueling, large separatrix densities can be achieved and the turbulent transport due to ballooning modes, which increases with density [28], can be large at the separatrix.

Table 3. Plasma and pedestal parameters for small ELM regimes in AUG and TCV, compared to parameters of the ITER baseline scenario assuming $T_{e,ped} = 4$ keV, $T_{e,sep} = 0.2$ keV, $n_{e,ped} = 0.7 \times 10^{20}$ m^{-3} and $n_{e,sep} = 0.3 \times 10^{20}$ m^{-3}.

	q_{95}	δ	Δ_{sep} (mm)	$\nu_{\star,ped}$	$\nu_{\star,sep}$	$f_{G,ped}$	$f_{G,sep}$
AUG (small ELM)	4.5	0.37	7	$\sim$1.4	$\sim$7	0.82	0.3
TCV (small ELM)	4.5	0.54	3	$\sim$2	$\sim$ 10	$\sim$0.35	$\geqslant$ 0.1
ITER	3	0.4	80	$\leqslant$0.1	$\sim$7	0.6–0.8	0.25

- This transport flattens the pressure profile around the separatrix, such that the remaining pedestal width, which determines the stability of the peeling-ballooning modes, becomes narrower. This has a stabilizing influence on type-I ELMs.

5. Conclusions and outlook

This paper reports on joint experiments conducted on AUG and TCV devices in order to assess the effect of plasma fueling and plasma shape on the onset of small ELM regimes (either type-II or grassy). We have clarified the key role of two parameters: the separatrix density and the magnetic shear in the immediate vicinity of the separatrix. In summary, for the onset of a small ELM regime:

- The plasma density at the separatrix must be large enough ($n_{e,sep}/n_G \geqslant 0.3$) to drive a large ballooning transport and therefore to flatten the pressure profile near the separatrix, which, finally, stabilizes type-I ELMs.
- The plasma triangularity has to be large enough ($\delta \geqslant 0.4$), which in practice, results in a magnetic configuration close to a double null (DN), parametrized with Δ_{sep}. This leads to a reduction of the magnetic shear in the extreme vicinity of the separatrix. As a consequence, its stabilizing effect on ballooning modes is weakened.

These critical parameters are reported in table 3 and compared to the ITER expected values [29, 30]. In this paper, it has been demonstrated that the onset of a small ELM regime strongly depends on the separatrix conditions. Therefore, it is important to realize that not only the ITER plasma shape but also the separatrix parameters $f_{G,sep}$ and $\nu_{\star,sep}$ can be matched in nowadays tokamaks. So, a small ELM regime with good confinement might be achievable in ITER. Nevertheless, since it is known that the ITER pedestal collisionality cannot be matched in present machines, a better physical understanding regarding the onset of a small ELM regime is needed to gain confidence on a possible extrapolation to ITER and beyond.

As it has been seen, type-I and small ELMs can exist at the same time, suggesting they are excited by different physical mechanisms. The underlying instabilities leading to grassy or type-II ELMs have been hypothesized to be ballooning modes located close to the separatrix, howerer further experiments devoted to a better understanding of the pedestal and SOL turbulence and particle and heat transport are required. This will be complemented by further development of theoretical models for small/no ELM regimes and by nonlinear MHD simulations using global codes in order to gain confidence in terms of their compatibility with ITER plasmas.

Finally, the effort to understand the physics of the small ELM regime will continue under the EUROfusion umbrella with further experiments on AUG, TCV and MAST-U in order to achieve small ELM regimes towards $q_{95} = 3$ [31] and ITER-relevant separatrix collisionalities.

Acknowledgments

This work has been carried out within the framework of the EUROfusion Consortium and received funding from the Euratom research and training programme 2014–2018 and 2019–2020 under Grant Agreeement No. 633053. The views and opinions expressed herein do not necessarily reflect those of the European Commission. G.F. Harrer is a fellow of the Friedrich Schiedel Foundation for Energy Technology. This work was supported in part by the Swiss National Science Foundation.

ORCID iDs

T. Eich https://orcid.org/0000-0003-3065-8420
G.F. Harrer https://orcid.org/0000-0002-1150-3987
L. Frassinetti https://orcid.org/0000-0002-9546-4494
R. Maurizio https://orcid.org/0000-0001-9896-6732
U. Sheikh https://orcid.org/0000-0001-6207-2489

References

[1] Sips A.C.C. *et al* (JET Contributors, The ASDEX Upgrade Team, The DIII-D Team, The C-Mod Team, The JT-60U Team, ITPA-IOS TG Members, and Experts) 2018 Assessment of the baseline scenario at $q_{95} \sim 3$ for ITER *Nucl. Fusion* **58** 126010
[2] Ozeki T., Chu M.S., Lao L.L., Taylor T.S., Chance M.S., Kinoshita S., Burrell K.H. and Stambaugh R.D. 1990 Plasma shaping, edge ballooning stability and ELM behaviour in DIII-d *Nucl. Fusion* **30** 1425–32
[3] Stober J., Maraschek M., Conway G.D., Gruber O., Herrmann A., Sips A.C.C., Treutterer W., Zohm H. and ASDEX Upgrade Team 2001 Type II ELMy H modes on ASDEX Upgrade with good confinement at high density *Nucl. Fusion* **41** 1123–34
[4] Oyama N. *et al* (The ITPA Pedestal Topical Group) 2006 Pedestal conditions for small ELM regimes in tokamaks *Plasma Phys. Control. Fusion* **48** A171–81
[5] Wolfrum E. *et al* (The ASDEX Upgrade Team) 2011 Characterization of edge profiles and fluctuations in discharges with type-II and nitrogen-mitigated edge localized modes in ASDEX Upgrade *Plasma Phys. Control. Fusion* **53** 085026
[6] Viezzer E. 2018 Access and sustainment of naturally ELM-free and small-ELM regimes *Nucl. Fusion* **58** 115002
[7] Harrer G.F. *et al* (The EUROfusion MST1 Team and The ASDEX Upgrade Team) 2018 Parameter dependences

of small edge localized modes (ELMs) *Nucl. Fusion* **58** 112001
[8] Kirk A. *et al* 2008 Comparison of the filament behaviour observed during type I ELMs in ASDEX upgrade and MAST *J. Phys.: Conf. Ser.* **123** 012012
[9] Hennequin P. *et al* (The ASDEX Upgrade Team and The EUROfusion MST1 Team) 2017 Inter-ELM fluctuations and flows and their evolution when approaching the density limit in the ASDEX Upgrade tokamak *Proc. of the 44th EPS Conf. on Plasma Physics (Belfast, UK, 26–27 June 2007)* (http://ocs.ciemat.es/EPS2017PAP/pdf/P1.167.pdf)
[10] Eich T., Goldston R.J., Kallenbach A., Sieglin B., Sun H.J., ASDEX Upgrade Team, and JET Contributors 2018 Correlation of the tokamak H-mode density limit with ballooning stability at the separatrix *Nucl. Fusion* **58** 034001
[11] Hawke J. *et al* 2017 Improving spatial and spectral resolution of TCV Thomson scattering *J. Instrum.* **12** C12005
[12] Groebner R.J. *et al* 2001 Progress in quantifying the edge physics of the h mode regime in DIII-d *Nucl. Fusion* **41** 1789–802
[13] Sheikh U.A., Dunne M., Frassinetti L., Blanchard P., Duval B.P., Labit B.P., Merle A., Sauter O., Theiler C., Tsui C., The TCV Team, and The EUROfusion MST1 Team 2019 Pedestal structure and energy confinement studies on TCV *Plasma Phys. Control. Fusion* **61** 014002
[14] Frassinetti L. *et al* (The ASDEX Upgrade Team, JET Contributors, The TCV Team, and The EUROfusion MST1 Team) 2019 Role of the pedestal position on the pedestal performance in AUG, JET-ILW and TCV and implications for ITER *Nucl. Fusion* **59** 076038
[15] Dunne M.G. *et al* (The EUROfusion MST1 Team, and The ASDEX Upgrade Team) 2017 Global performance enhancements via pedestal optimisation on ASDEX Upgrade *Plasma Phys. Control. Fusion* **59** 025010
[16] Reimerdes H. *et al* 2017 TCV divertor upgrade for alternative magnetic configurations *Nucl. Mater. Energy* **12** 1106–11
[17] Kamada Y., Oikawa T., Lao L., Takizuka T., Hatae T., Isayama A., Manickam J., Okabayashi M., Fukuda T. and Tsuchiya K. 2000 Disappearance of giant ELMs and appearance of minute grassy ELMs in JT-60U high-triangularity discharges *Plasma Phys. Control. Fusion* **42** A247–53
[18] Stober J., Gruber O., Kallenbach A., Mertens V., Ryter F., Stäbler A., Suttrop W., Treutterer W. and The ASDEX Upgrade Team 2000 Effects of triangularity on confinement, density limit and profile stiffness of H-modes on ASDEX Upgrade *Plasma Phys. Control. Fusion* **42** A211–6
[19] Maurizio R., Elmore S., Fedorczak N., Gallo A., Reimerdes H., Labit B., Theiler C.K., Tsui C., Vijvers W., The TCV Team, and The MST1 Team 2018 Divertor power load studies for attached L-mode single-null plasmas in TCV *Nucl. Fusion* **58** 016052
[20] Eich T., Andrew P., Herrmann A., Fundamenski W., Loarte A., Pitts R.A. and JET-EFDA Contributors 2007 ELM resolved energy distribution studies in the JET MKII gas-box divertor using infra-red thermography *Plasma Phys. Control. Fusion* **49** 573–604
[21] Merle A., Sauter O. and Medvedev S.Y. 2017 Pedestal properties of H-modes with negative triangularity using the EPED-CH model *Plasma Phys. Control. Fusion* **59** 104001
[22] Kallenbach A., Asakura N., Kirk A., Korotkov A., Mahdavi M.A., Mossessian D. and Porter G. 2005 Multi-machine comparisons of H-mode separatrix densities and edge profile behaviour in the ITPA SOL and Divertor Physics Tpical Group *J. Nucl. Mater.* **337–9** 381–5
[23] Stangeby P.C. 2000 *The Plasma Boundary of Magnetic Fusion Devices* (Bristol: Institute of Physics)
[24] Dunne M.G. *et al* (The EUROfusion MST1 Team, and The ASDEX-Upgrade Team) 2017 The role of the density profile in the ASDEX-Upgrade pedestal structure *Plasma Phys. Control. Fusion* **59** 014017
[25] Lütjens H., Bondeson A. and Sauter O. 1996 The CHEASE code for toroidal MHD equilibria *Comput. Phys. Commun.* **979** 219–60
[26] Halpern F.D., Jolliet S., Loizu J., Mosetto A. and Ricci P. 2013 Ideal ballooning modes in the tokamak scrape-off layer *Phys. Plasmas* **20** 052306
[27] Rogers B.N., Drake J.F. and Zeiler A. 1998 Phase space of tokamak edge turbulence, the L-H transition, and the formation of the edge pedestal *Phys. Rev. Lett.* **81** 4396–9
[28] Scott B. 1997 Three-dimensional computation of drift Alfvén turbulence *Plasma Phys. Control. Fusion* **39** 1635
[29] Kukushkin A., Pacher H., Kotov V., Pacher G. and Reiter D. 2011 Finalizing the ITER divertor design: the key role of SOLPS modeling *Fusion Eng. Des.* **86** 2865–73
[30] Loarte A. *et al* (The ITPA Scrapeoff Layer Group, and Diver) 2007 Chapter 4: power and particle control *Nucl. Fusion* **47** S203–63
[31] Pütterich T. *et al* (The EUROfusion MST1 Team and The ASDEX Upgrade Team) 2018 The ITER Baseline Scenario investigated at ASDEX Upgrade *Preprint: 2018 IAEA Fusion Energy Conf. (Gandhinagar, India, 22–27 October 2018)* EX/P8-4